

# Occurrence and scale of compositional heterogeneity in Martian dune fields: Toward understanding the effects of aeolian sorting on Martian sediment compositions



Cong Pan<sup>a,b,\*</sup>, A. Deanne Rogers<sup>a</sup>

<sup>a</sup> Department of Geosciences, Stony Brook University, 255 Earth and Space Sciences Building, Stony Brook, NY 11794-2100 USA

<sup>b</sup> Department of Earth, Planetary, and Space Sciences, University of California, Los Angeles, CA 90095-1567 USA

## ARTICLE INFO

### Article history:

Received 18 March 2016

Revised 6 September 2016

Accepted 9 September 2016

Available online 22 September 2016

### Keywords:

Mars

Composition

Remote sensing

Dune

Thermal inertia

Aeolian sorting

## ABSTRACT

Aeolian transport and hydrodynamic sorting have been proposed to be a significant influence on Martian sediment bulk compositions, through laboratory experiments, modeling and terrestrial analogies. But to date, few studies have directly examined compositional-grain size relationships within sediment fields on Mars; thus the prevalence of hydrodynamic sorting as well as the scales at which sorting is important remain poorly understood. To that end, we assessed the degree and occurrence of thermophysical and compositional heterogeneity for 25 dune fields within a ~42,000,000 km<sup>2</sup> area on Mars. Among these, only four exhibit spatial heterogeneity in spectral properties and composition. Two of these four sites show a strong positive relationship between particle size and olivine abundance. The rarity of compositional heterogeneity within dune fields in our study region (5–185°E, 45°N–20°S) may indicate phenocryst-poor source rocks; alternatively, sorting within individual bedforms may be present but not at the scale of the full dune field (~10–20 km). Compositional segregation correlated with grain size due to hydrodynamic sorting has been observed by rovers at scales much smaller than THEMIS ground resolution (100 m/pixel); thus these small scales might be the operable, relevant ones of hydrodynamic compositional sorting prevailing most commonly in Martian dune fields.

© 2016 Elsevier Inc. All rights reserved.

## 1. Introduction

Interpretation of sediment compositions from remote measurements requires consideration of a variety of factors, including source rock properties, chemical and mechanical alteration, transport history, and sorting processes. Presently, major questions regarding Martian sediments and aeolian processes relate to the degree to which sediments have been compositionally homogenized by aeolian, impact and other processes, and conversely, the role that physical sorting plays in generating compositional variations with particle size. The similarity in chemical compositions of basaltic sediments at Gale crater, Gusev crater and Meridiani Planum, measured in-situ by landed missions, has prompted the hypothesis of a “global” soil unit (Blake et al., 2013; Yen et al., 2005), in which sand-sized particles have been globally homogenized through aeolian activity (Blake et al., 2013). An alternative model is that basaltic soils are not globally homogenized, but sample a large enough area to approximate average upper crust (Taylor and McLennan, 2009, p.159). This latter idea is more con-

sistent with global measurements of surface compositions from infrared and gamma ray measurements that show significant spatial variability at the regional scale (e.g. Karunatillake et al., 2010; Ody et al., 2012; Rogers and Christensen, 2007; Rogers and Hamilton, 2015; Taylor et al., 2010; Pan et al., 2015), indicating that complete homogenization of the sediment fraction has not occurred (Rogers and Hamilton, 2015). However, it is possible that homogenization occurs within a restricted size range of the saltatable fraction, where smaller sediments are physically separated from larger ones and homogenized at larger scales.

Additional motivation for this work stems from the need to understand the origin(s) of spatially isolated bedrock compositions. For example, numerous ancient craters and basins on Mars, ranging from ~8–130 km diameter (average diameter of ~42 km) (Edwards et al., 2014) contain flat-lying olivine-enriched bedrock plains (Edwards et al., 2009, 2014; McDowell and Hamilton, 2007). Potential origins for these units include effusive volcanism and/or lithified sedimentary fill (McDowell and Hamilton, 2007; Edwards et al., 2009, 2014). If these units are sedimentary, there must be a mechanism to enrich the sedimentary deposits in olivine compared to surrounding terrains (the presumed sediment sources). Aeolian sorting is one potential way to do this.

\* Corresponding author.

E-mail address: [pancong419@gmail.com](mailto:pancong419@gmail.com) (C. Pan).

Thus, understanding the potential role of physical sorting in controlling bulk sediment composition is an important facet in interpreting observed spatial variability in surface compositions from orbit. Though the processes that result in compositional fractionation from a bulk source during erosion and aeolian transport are generally well understood from the terrestrial literature (Section 2), it is unclear under what scales these processes are important on Mars, as well as how these changes might appear on surfaces dominated by basaltic sources. Dune and ripple fields are natural environments in which to assess the degree to which physical sorting processes have affected Martian sediments. Martian sediments investigated *in-situ* with landed missions show evidence of compositional and grain size sorting over the scale of individual bedforms (e.g. McGlynn et al., 2011; Sullivan et al., 2008). At slightly larger scales, such as within a portion of the informally named “Bagnold” dune field in Gale crater, spatial variability in mineral composition and grain size has been observed remotely (Lapotre et al., 2015; Seelos et al., 2014). Additionally, prior infrared mapping studies of Martian dune fields and nearby bedrock provide evidence that many dune field compositions are at least partially controlled by local inputs (e.g., Chojnacki et al., 2014a; Tirsch et al., 2011). However, studies across larger areas, such as a whole dune field, have been limited. A comprehensive study of dune fields within Valles Marineris showed significant compositional heterogeneity at multiple scales, with major differences in mineralogy between individual basins within Valles Marineris, as well as compositional differences observed between individual dune fields (Chojnacki et al., 2014a,b). Those authors suggested that the diversity of sand sources within Valles Marineris contributed to the regional differences in dune field composition, whereas aeolian sorting was likely the more dominant factor in the smaller scale variability observed. However, aside from that study, as well as the *in-situ* observations at few landing sites, detailed analyses of heterogeneity (or lack thereof) within other Martian dune fields, as well as an assessment of composition-particle size relationships, are generally lacking (Section 2).

Thermal infrared imaging from the Mars Odyssey Thermal Emission Imaging System (THEMIS) instrument (Christensen et al., 2004) provides a means to assess spatial variability in spectral and thermophysical characteristics that are related to composition and particle size (Section 3). Though the coarse spectral resolution prevents precise determination of mineralogy, the uniform spatial coverage at high spatial resolution (100 m/pixel) uniquely allows assessment of spatial heterogeneity in bulk composition and particle size across regions of interest. This work complements previous studies by using visible and infrared imagery from THEMIS to assess the frequency of thermophysical and spectral heterogeneity within dune fields in an equatorial region of Mars, and then characterizing compositional-particle size relationships in the spectrally heterogeneous dune fields.

## 2. Background

Variations in composition and particle size distributions within aeolian dune fields on Earth are a function of source rock composition(s), mechanical and chemical weathering, and aeolian sorting mechanisms (Boggs, 2006, p. 145–157, 258–267). The original crystal size and composition of source rock(s) first influence the grain size and composition of sediments derived from those rocks (Pettijohn et al., 1987, p. 252–254). Preferential comminution and chemical alteration can change the composition of those sediments, as a function of grain size, during transport. Finally, aeolian sorting of particles leads to preferential enrichment of specific materials in certain grain-size fractions (e.g. Tolosana-Delgado and von Eynatten, 2009; Weltje and von Eynatten, 2004). Grain size, shape and density are major factors controlling the

effectiveness of aeolian sorting (e.g. Anderson and Bunas, 1993; Makse, 2000). Grain sizes are commonly segregated within individual dune fields, with coarse-grained ripple crests and finer-grained troughs (Anderson and Bunas, 1993).

On Earth, the protolith composition of the sand source has been shown to have a major role in affecting compositional sorting trends within sediments derived from that source. Because the common rock-forming minerals in basaltic rocks can have a wide range of densities compared to intermediate and silicic rocks, the effects of hydraulic sorting on compositional trends with particle size in basaltic sediments can differ greatly from those of intermediate-to-silicic sediments (e.g., Kiminami and Fujii, 2007). Unfortunately, studies of aeolian sorting in basaltic terrains are rare. Spatial variations in chemical and mineralogical composition were observed in volcanic sands in Iceland, such that sands showed enrichments in olivine compared to the source rock; and, within the sediments, olivine abundance (by way of Ni abundance as a proxy for olivine abundance) increased with decreasing mean grain size (Mangold et al., 2011). The negative correlation between olivine abundance and particle size was explained by olivine shape, hardness and density leading to longevity as sand-sized particles compared to plagioclase. In the basaltic terrains surrounding Moses Lake, Washington, dune crests were observed to be compositionally dissimilar from the remaining dune field surfaces in remotely sensed infrared data (Bandfield et al., 2002). In this example, however, the differences were due to distinct sand sources, followed by aeolian sorting, rather than preferential comminution from a single sand source. Last, particle size sorting can occur with density variations related to porosity/vesicularity, which is expected for basaltic terrains. Density-related particle size sorting has been observed in granule mega-ripples in Iceland and Mono Crater, where the high density and finer obsidian grains formed the crests and the low density and coarser pumice was concentrated between the crests (e.g. Greeley and Peterfreund, 1981).

Despite the limited number of terrestrial examples of sorting in basaltic terrains (e.g. Edgett and Lancaster, 1993), combined experimental and modeling work on basaltic sediments suggests that physical processes could produce significant compositional changes in Martian sediments from a single protolith (Fedó et al., 2015). In that study, two basalt samples differing in composition and petrographic texture were crushed and pulverized to generate synthetic sediments (Fedó et al., 2015). The two samples were a trachybasalt from Cima volcanic field in Mojave Desert, California and porphyritic vesicular basalt from Kilauea, Hawaii. Samples were sieved into multiple grain-size fractions; particles finer than 62  $\mu\text{m}$  were not further subdivided. The mineral abundance of sieved sediments and source rocks was determined and divided into five groups: lithic fragments, olivine, plagioclase and pyroxene and opaque oxides. The compositions of the sieve fractions differed greatly with starting composition. They concluded that the crystal-size distribution of the parent material had a major influence on the compositional variability between grain size fractions. Next, using aeolian transport models, Fedó et al. (2015) showed that these compositionally distinctive size fractions could then be spatially sorted through hydrodynamic processes under Martian atmospheric conditions. They conclude that physical sorting should be likely on Mars, and that sorting is a process that should not be overlooked when assessing chemical or mineralogical variability in Martian sediments. However, the hydrodynamic effects related to density differences within basaltic sediments, which are expected to vary by nearly a factor of two among common minerals (e.g., plagioclase vs. Fe-oxides), may have been lost or conflated during the processes of sieving, thus the likelihood of physical sorting remains unclear.

Some well-characterized dune or ripple fields on Mars do show evidence for sorting. The “El Dorado” ripple field investigated by

the Spirit Rover is characterized by olivine-enriched coarse grains and pyroxene-enriched fine grains (Sullivan et al., 2008). They speculated both types of sand were derived from a single original basalt composition, where particles dominated by one or more phenocrysts of olivine abraded more slowly due to the hardness and conchoidal fracture compared with less durable pyroxene. Similarly, in Valles Marineris dune fields, evidence from thermal data suggested that sediment with olivine as the dominant mineral consisted of larger particle sizes than sediments dominated by pyroxene, glass, or other minerals (Chojnacki et al., 2014b). The Bagnold dune field within Gale crater exhibits spatial differences in olivine and high-calcium pyroxene band strengths, likely caused by aeolian grain sorting (Seelos et al., 2014). Last, from thermal orbital data of the dune field within Proctor Crater, smaller particle sizes were inferred for the interdunes and the dune troughs relative to the dune crests (Fenton and Mellon, 2006). In this case, rather than sorting, the preferred interpretation was that sand saltation may only be effective enough to keep the dunes crests themselves clear of dust while the interdunes and troughs are not as dust free as crests (Fenton and Mellon, 2006). These remote sensing and in situ studies provide a framework in which to evaluate our Mars observations.

### 3. Data and methods

#### 3.1. Overview of approach

Dune fields within impact craters located between (45°N, 5°E) and (20°S, 185°E) were initially included as candidate areas for study. The study region includes a variety of terrain types, ages, and elevations. Dune fields within the study region were identified by using the Mars Global Digital Dune Database (Hayward et al., 2014), but additional low albedo deposits within craters were also examined. Albedo and dust cover index (DCI) (Ruff and Christensen, 2002) derived from the Mars Global Surveyor Thermal Emission Spectrometer (TES) instrument ( $3 \times \sim 8$  km per pixel, Christensen et al., 2001) were used to infer the dust level on the dune fields in this study. Dune fields with DCI values smaller than 0.962 were considered to be dust-covered (Ruff and Christensen, 2002). Because dust cover obscures the spectral properties of the underlying dune sands, surfaces with high dust cover were excluded from compositional analysis.

First, each dune field was closely inspected with high-resolution visible imagery from the Mars Reconnaissance Orbiter Context Imager (CTX) instrument ( $\sim 6$  m/pixel) (Malin et al., 2007), to assess the degree of sand cover continuity within the sand deposit or dune field. Assessment of sand cover continuity is important because significant interdune surfaces or rocky protrusions (e.g. buttes, small crater rims) could confound attempts to identify compositional and particle size trends in only the dune sands present.

Next, each dune field was independently examined for thermophysical (Section 3.2) and spectral (Section 3.3) heterogeneity using THEMIS thermal infrared data (100 m/pixel) (Christensen et al., 2004). Then, for the dune fields with contiguous sand cover, spectral data from THEMIS and (where available) the Mars Reconnaissance Orbiter Compact Reconnaissance Imaging Spectrometer for Mars (CRISM, Murchie et al., 2007) were analyzed to discern relationships between thermophysical and compositional properties. High spatial resolution visible images from CTX were used to define the boundaries of dune fields and characterize the dune field morphology of spectrally or physically distinct units identified by THEMIS.

#### 3.2. Thermal inertia and particle size

Thermal inertia is the measurement of a material's resistance to changes in temperature, and can be related to the average particle

size of a surface (Chojnacki et al., 2011; Fergason et al., 2006; Kieffer et al., 1977; Presley and Christensen, 1997). Thermal inertia is defined as

$$I = (k \rho c)^{1/2} \quad (1)$$

where  $k$  is the thermal conductivity,  $\rho$  is the bulk density of the surface material and  $c$  is the specific heat. Values of  $\rho$  and  $c$  vary by a factor of  $\sim 2$ – $3$  for most geologic materials, but under Martian atmospheric conditions, for non-indurated particulate surfaces on Mars, variations in thermal inertia depend primarily on the mean particle size of the surface, which affects the thermal conductivity (Edgett and Christensen, 1991; Jakosky, 1979). In this work, data from THEMIS band 9 (Christensen et al., 2004) were used to assess thermal inertia variations within each dune field, at a resolution of 100 m/pixel. THEMIS-derived thermal inertia images (Christensen et al., 2013; Fergason et al., 2006) from nighttime, low dust opacity observing conditions over each region were selected for analysis using JMARS, a publically-available GIS data server (<http://jmars.asu.edu>). Effective particle sizes were determined from thermal inertia by first finding  $k$  using Eq. (1) and a value of  $1 \times 10^6 \text{ J m}^{-3} \text{ K}$  for the product of  $\rho$  and  $c$  (Christensen et al., 2001; Fergason et al., 2006). Next, the experimentally determined relationship between thermal conductivity and particle diameter for 5 torr (the average pressure of the Martian surface) (Presley and Christensen, 1997):

$$k = (C P^{0.6}) d^{((-0.11 * \log(P/K)))} \quad (2)$$

was used to derive an effective particle size ( $d$ ) (Kieffer et al., 1973). In Eq. (2),  $C$  and  $K$  are the constants 0.0015 and 81,000 torr (Presley and Christensen, 1997),  $P$  is atmospheric pressure (5 torr) and  $d$  is the particle diameter in  $\mu\text{m}$ . Only areas with thermal inertia between 164 and 365  $\text{J m}^{-2} \text{ s}^{-0.5} \text{ K}^{-1}$ , corresponding to sand-sized sediments using the above  $\rho c$  value, were included for further thermal inertia and composition analysis (Presley and Christensen, 1997).

We note that, because we are investigating dune fields with potential for compositional sorting, variations in  $\rho$  are possible, independent of variations in grain size. To investigate the effects of varying bulk density on grain size estimates, we calculated the thermal inertia values for two different  $\rho c$  products:  $1 \times 10^6$  and  $0.80 \times 10^6 \text{ J m}^{-3} \text{ K}$ , while keeping grain size constant and using  $k$  values from Presley and Christensen (1997). The spread was chosen based on spread in bulk density observed from Viking- and Pathfinder-based estimates of  $\rho$ , which varied between  $\sim 1.2$  and  $1.5 \text{ g/cm}^3$  (Moore et al., 1987, p. 130, 1999), a difference of approximately 20%. Next, using those thermal inertia values, we determined the grain size using the standard value of  $1 \times 10^6 \text{ J m}^{-3} \text{ K}$  for  $\rho c$ . We find that this leads to differences ranging from  $\sim 50$ – $700 \mu\text{m}$  in thermal inertia-derived particle diameter estimates for thermal inertia values between 200–365  $\text{J m}^{-2} \text{ s}^{-0.5} \text{ K}^{-1}$ , with the highest differences corresponding to the highest thermal inertia value in that range (e.g. particle diameter estimates varied by  $\sim 50 \mu\text{m}$  for a thermal inertia value of 200  $\text{J m}^{-2} \text{ s}^{-0.5} \text{ K}^{-1}$ ). These differences are very large; however, we argue that a combination of invariant particle size and variant bulk density is extremely unlikely. Regardless, any thermophysical heterogeneity observed would indicate variations in one or both of these parameters, providing evidence for sorting. Variations in thermal inertia trends, rather than absolute grain sizes, are the focus of this study.

#### 3.3. Compositional analysis

Analysis of compositional heterogeneity was carried out using infrared spectral images from THEMIS. Decorrelation stretched (DCS) THEMIS daytime thermal infrared multispectral images, with surface temperatures  $> 250 \text{ K}$ , were used to preliminarily assess

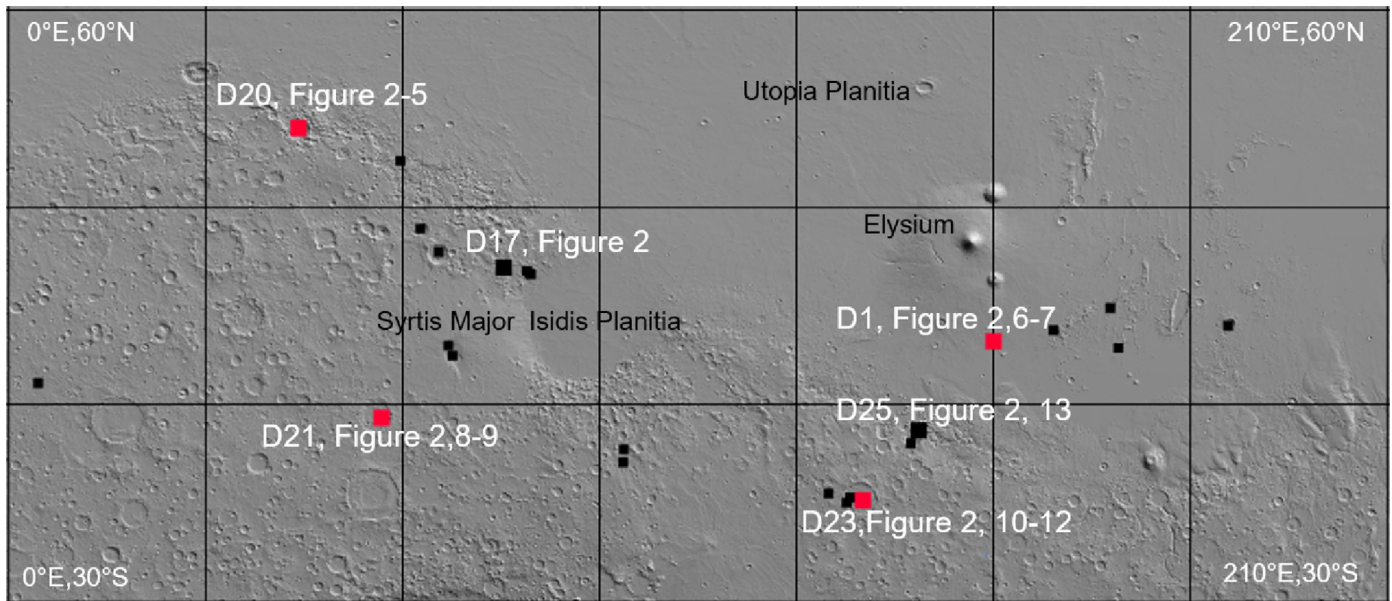


**Fig. 1.** Distribution of dune fields in this study. The larger red and black squares are dune fields with contiguous sand cover and that were analyzed in detail. The red squares are dune fields exhibiting clear spatial heterogeneity in spectral properties in THEMIS imagery. (For interpretation of the references to color in this figure legend, the reader is referred to the web version of this article.)

whether spatial heterogeneity in composition was present within each dune field (indicated by color variations within the stretch). It is important to note that DCS images, because they are stretched, can produce “false positives” when assessing spectral variability, but not “false negatives.” Lack of color variation in a DCS image is a good indicator of spectral uniformity (e.g. Gillespie et al., 1986). Potential areas of compositional distinction highlighted with the DCS images were further analyzed quantitatively by extraction of surface emissivity from regions of interest identified within the scene. To extract emissivity spectra, instrument artifacts and atmospheric influences were corrected using the methods described by Bandfield et al. (2004). As will be shown, much of the spectral variation can be described using varying amounts of olivine (Section 4). Thus to map compositional variations quantitatively across the scene, linear spectral unmixing (Bandfield et al., 2004) using scene-derived olivine-poor and laboratory olivine emissivity spectra as end-members was applied to each THEMIS pixel over the dune field. Even where olivine abundances are low, the use of these two endmembers (with minima at  $\sim 9$  and  $11 \mu\text{m}$ ) can adequately capture any variability in silicate composition within the scene, because varying silicate composition produces a measurable change in the position of the emissivity minimum between  $\sim 9$ – $11 \mu\text{m}$ . Olivine concentrations are normalized for blackbody, which allows for adjustments based on overall spectral depth (e.g. Hamilton et al. 1997), and presented as areal abundance (0–100%). Last, THEMIS-derived spectral images and nighttime images were co-registered to directly compare spectral properties (including olivine abundance) and thermal inertia. Images were classified based on 20th percentile thermal inertia intervals and olivine abundance values and emissivity spectra were retrieved for each thermal inertia interval. Comparisons by thermal inertia interval, rather than pixel-to-pixel, were used due to the possibility of sub-pixel mixing and/or slight pixel mis-registration between day and nighttime images.

CRISM is a hyperspectral imaging spectrometer with 544 channels covering the visible to near-infrared spectral region from 0.4 to  $4.0 \mu\text{m}$  at  $6.55 \text{ nm}$  spectral sampling and a nominal spatial resolution of  $\sim 18 \text{ m}$  or  $40 \text{ m/pixel}$  (Murchie et al., 2007). Spectral indices derived from atmospherically corrected (McGuire et al.,

2009) CRISM targeted images, as well as laboratory spectra from the CRISM spectral library, were used to identify the presence and distribution of olivine, low-calcium pyroxene, high-calcium pyroxene, hydrated minerals (Viviano-Beck et al., 2014) and glass (Horgan and Bell, 2012). The CRISM spectral indices were used to find the locations of strongest signatures of these minerals, and average reflectance spectra were extracted from those locations. If possible, the average spectrum was then ratioed with a spectrally neutral surface (a dusty region) within the scene, along the same detector column, to minimize residual atmospheric absorptions and better highlight the spectral characteristics of the region of interest. The Mars Express Observatoire pour la Minéralogie, l’Eau, les Glaces et l’Activité (OMEGA) instrument (Bibring et al., 2004), an imaging spectrometer with comparable spectral range to CRISM, was not used in this study due to its coarser spatial resolution.

## 4. Results

### 4.1. Overview

Within the study region, 25 candidate dune fields were identified (Fig. 1). All of the dune fields are within impact craters, which are major accumulation sites for sediment. Of the 25 sites studied, only four were found to exhibit clear spatial heterogeneity in spectral properties in THEMIS imagery (Fig. 1). All four of these sites exhibited contiguous sand coverage in CTX imagery, indicating that the spectral variability can be attributed to variations within the sediment fraction. These sites also exhibited spatial variability in thermal inertia values; compositional-particle size relationships are described in detail for these four sites in Section 4.2.

The remaining 21 spectrally-homogeneous sites all exhibited intra-field variability in thermal inertia, but upon closer inspection with visible imagery, only two were found to exhibit adequate continuity of sand surface coverage such that the thermal inertia variations could be attributed to variations in particle size within the sediment component (Section 3). We note that, though interdune surfaces would prevent us from drawing conclusions about observed heterogeneity in spectral properties, a lack of spectral

**Table 1**  
Location and characteristics of dune fields with contiguous sand coverage.

Dune field ID	D1	D20	D21	D23	D17	D25
Latitude	9.5°N	42.2°N	-2.1°N	-14.3°N	20.8°N	-5.0°N
Longitude	150.0°E	44.3°E	57.0°E	128.5°E	75.6°E	137.0°E
TES albedo	0.11	0.12	0.11	0.10	0.13	0.21
TES dust index	0.970	0.977	0.976	0.976	0.973	0.965
Thermal inertia ( $\text{J m}^{-2}\text{s}^{-0.5}\text{K}^{-1}$ )	280–365	164–220	225–332	190–240	202–296	234–365
Effective particle size	639–2000 $\mu\text{m}$	63–226 $\mu\text{m}$	249–1333 $\mu\text{m}$	120–328 $\mu\text{m}$	156–812 $\mu\text{m}$	294–2000 $\mu\text{m}$
Figure numbers	Figs. 2,6–7	Figs. 2–5	Figs. 2,8–9	Figs. 2,10–12	Fig. 2	Fig. 13
Crater name	–	Moreux	–	–	Hargraves	Gale
CRISM IDs	No data coverage	HRL0000BEC3	No data coverage	FRT0000BE81 HRS00002FC0	No data coverage	FRT0000C518
THEMIS Daytime IDs						
IDs	I10480013	I01122002	I01708010	I17619022	I47821006	I01855008
THEMIS nighttime IDs	I06168009	I06908010	I07869014	I07180008	I18574010	I05459012

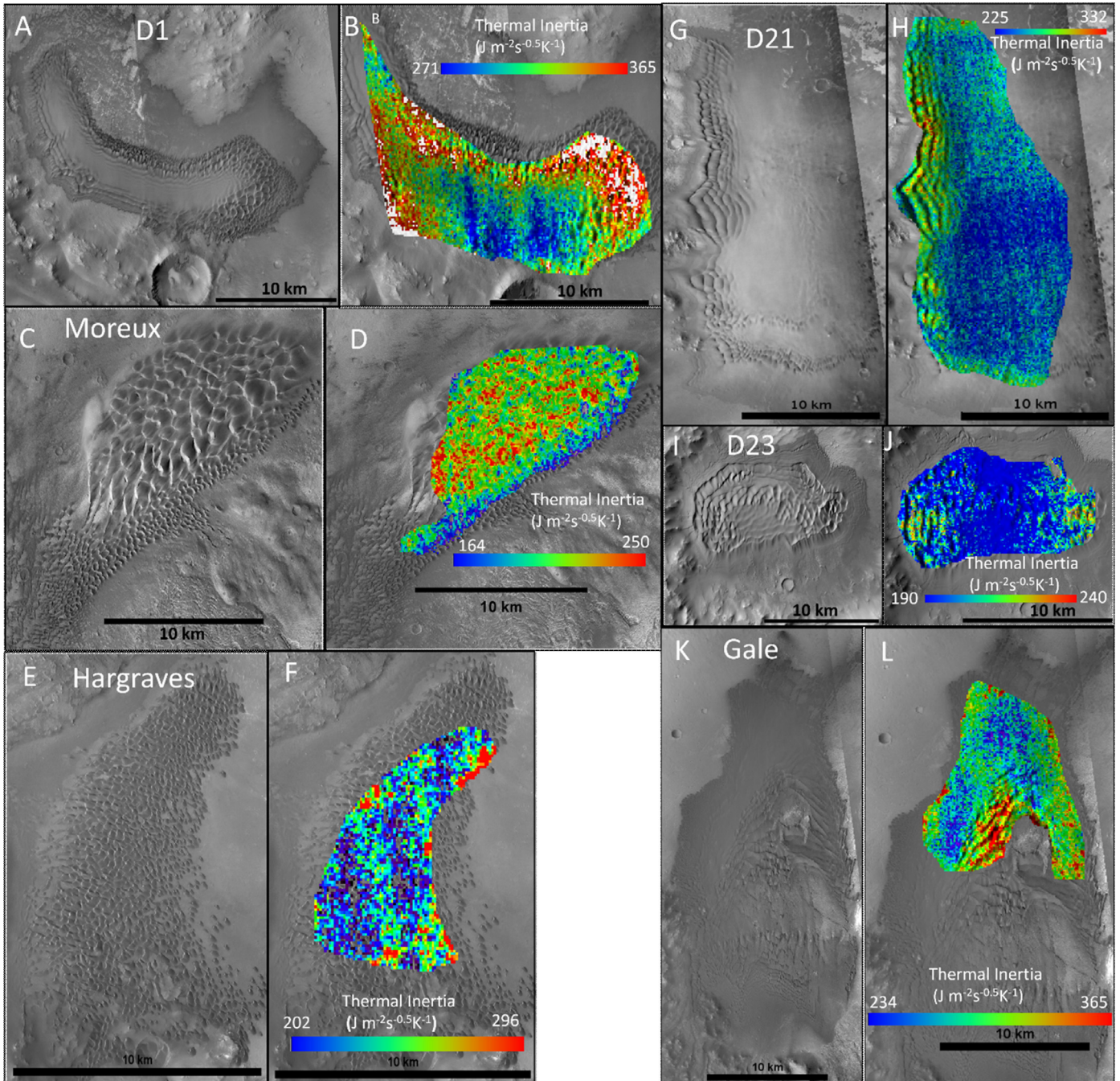


**Fig. 2.** Morphology and thermal inertia distributions for dune fields with contiguous sand cover listed in Table 1. CTX images are shown in A, C, E, G, I and K. THEMIS thermal inertia images superposed over CTX images are shown in B, D, F, H, J and L. Only the portions of the dune fields with contiguous sand cover in CTX were analyzed.

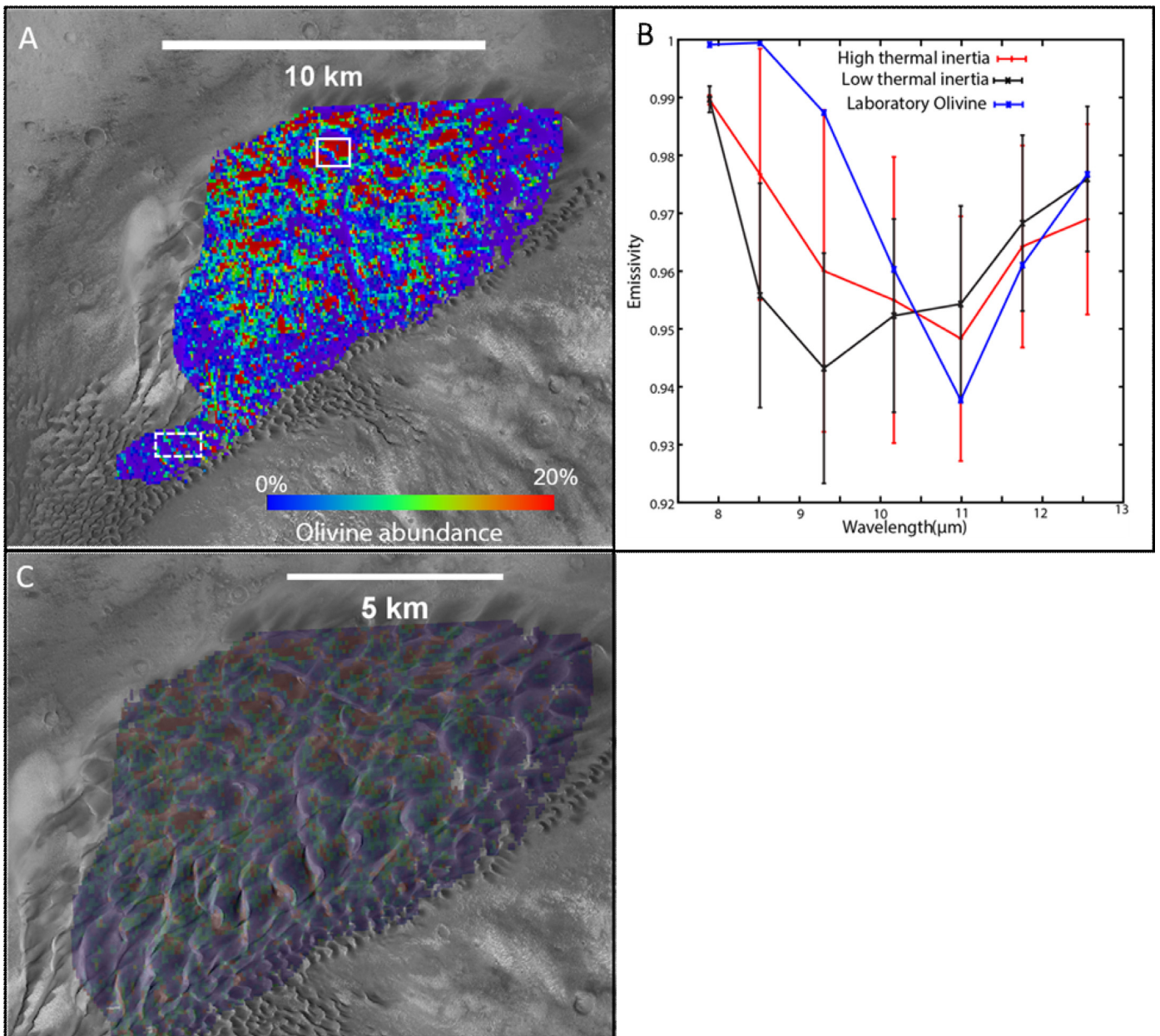


**Fig. 3.** THEMIS-derived olivine abundance of dune field in Moreux crater (site D20). A. THEMIS derived olivine abundance superposed over CTX images. White polygons indicate locations of spectral extraction in B; solid=high thermal inertia region, dashed=low thermal inertia region. B. Average THEMIS spectra from high and low thermal inertia parts of the dune field. Laboratory spectrum of olivine is plotted for reference. Spectra are offset for clarity. C. THEMIS olivine abundance map overlain on CTX map showing a closer view of the olivine distribution with morphology. Color scale is same as for B. (For interpretation of the references to color in this figure legend, the reader is referred to the web version of this article.)

variability like indicates that the dune field sediments are spatially homogeneous. Thus despite the prevalence of interdune surfaces among the 25 sites studied, we can conclude that intra-field spectral variations are rare within dune field sediments in our study region, at the scale that can be resolved by THEMIS (100 m/pixel).

For the remainder of this paper, we focus on the six sites with spatial contiguity in sediment cover (Table 1). Thermal inertia values within these dune fields range from  $164 \text{ J m}^{-2} \text{ s}^{-0.5} \text{ K}^{-1}$  to  $365 \text{ J m}^{-2} \text{ s}^{-0.5} \text{ K}^{-1}$ , indicating very fine sand to very coarse sand (Presley and Christensen, 1997). With the exception of the Gale crater site, TES albedo values of these dune fields range from 0.1 to 0.15 and TES dust cover index values range from 0.970 to 0.977 (Ruff and Christensen, 2002), suggesting dust free and likely active surfaces. In Gale, TES albedo and dust cover index values are  $\sim 0.21$  and  $\sim 0.965$  respectively, suggesting slightly higher dust cover.

## 4.2. Compositional-particle size relationships in Moreux, D1, D21, and D23

### 4.2.1. Moreux crater (site D20)

The thermal inertia values of the Moreux crater dune field range between  $164$  to  $220 \text{ J m}^{-2} \text{ s}^{-0.5} \text{ K}^{-1}$ , indicating grain sizes between  $\sim 60$ – $230 \mu\text{m}$ . These values are shifted to a lower range than the average thermal inertia value of  $230 \text{ J m}^{-2} \text{ s}^{-0.5} \text{ K}^{-1}$  reported for this dune field by Edgett and Christensen (1994) using Viking Orbiter Infrared Thermal Mapper (IRTM) (Kieffer et al., 1977) data. The differences are likely due to the difference in spatial resolution (35 km/pixel as opposed to 100 m/pixel) and/or to potential differences in atmospheric dust opacity between observations. From CTX imagery (Fig. 2A), we observe larger dunes and draas with well-defined slip faces and crescents in the northeastern part of

the site, whereas the remainder of the field exhibits smaller bedforms and fewer slip faces. The thermal inertia range of the large dune portion is higher than the small bedform portion, indicating a decrease of effective particle size in the small bedform portion (Fig. 2B). Though derived thermal inertia can be affected by surface slope and aspect angle (Jakosky, 1979), we observe little evidence that this is a strong factor influencing the spatial variability in thermal inertia in this region, because the high thermal inertia areas (as well as olivine concentrations, described below) are concentrated both on lee and stoss sides, and in the crests as well as low-lying troughs (Figs. 2 and 3).

The average THEMIS spectrum of the high thermal inertia portion exhibits low emissivity at  $\sim 11\mu\text{m}$  relative to  $\sim 9\mu\text{m}$ , consistent with increased olivine abundance (e.g., Hamilton and Christensen, 2005) (Fig. 3). Conversely, the low thermal inertia portion of the dune field exhibits absorption at  $\sim 9\mu\text{m}$  and lacks a strong  $11\mu\text{m}$  absorption, consistent with olivine poor materials. A THEMIS-derived olivine abundance map confirms this trend (Fig. 3). The CRISM spectral parameter image (Fig. 4) also shows spatially variable olivine signatures within the Moreux crater dune field, with stronger olivine index values in the large bedform part, and a deeper absorption near  $\sim 1.2\mu\text{m}$  (Fig. 4). The stronger  $\sim 1.2\mu\text{m}$  absorption can indicate higher olivine abundance and/or smaller particle size (Hapke, 1993; Salisbury, 1993).

The correlation between thermal inertia and composition is present across much of the dune field (Fig. 5). Average THEMIS spectra from increasing thermal inertia intervals show a shift in the position of the major absorption feature to higher wavelengths, indicating increase of olivine abundance. Though there is quite a bit of variability within these intervals, indicated by the standard deviations, a general trend of increasing olivine with particle size is present.

#### 4.2.2. Site D1

The thermal inertia range of the dune field at Site D1 is relatively higher than other sites, and indicates very coarse sands (Table 1). Within the dune field, some areas were masked prior to further analysis, due to their high thermal inertia ( $>365\text{ J m}^{-2}\text{ s}^{-0.5}\text{ K}^{-1}$ ) that suggests materials with particle size larger than sand materials (Fig. 6). The thermal inertia distribution within D1 suggests that particle sizes near the dune field perimeter, which has larger bedforms, are coarser than those near the center of the dune field and sand sheet (Fig. 6). As with Moreux crater, higher thermal inertia regions exhibit lower  $\sim 11\mu\text{m}$  emissivity values than lower thermal inertia areas, suggesting differences in olivine abundance with thermal inertia (Fig. 7). Also similar to Moreux, this trend of increasing olivine with particle size is present across much of the dune field (Fig. 7B and 7C). However, the differences in olivine abundance and THEMIS spectral characteristics (Fig. 7D) between thermal inertia ranges are not as large as those within Moreux. Significant variability within each interval is also present.

#### 4.2.3. Site D21

Thermal inertia values within Site D21 range from  $225\text{--}332\text{ J m}^{-2}\text{ s}^{-0.5}\text{ K}^{-1}$  (Table 1). Transverse and barchanoid dune field types with large slip faces are in the west and south of D21, whereas the remainder of the dune field is smoother, with muted slip faces, and exhibits sand sheet morphology (Figs. 2G and 2H). These latter areas also exhibit lower thermal inertia values, indicating a decrease of effective particle size (Figs. 2G and 2H). Though sand sheets in other locations of Mars commonly show evidence for increased dust cover (Chojnacki et al., 2014a,b), no differences in TES albedo or DCI are observed between the sand sheet and other dune morphologies in the field.

Although olivine abundance across the dune field is low compared to Moreux and D1, there are spectral differences between

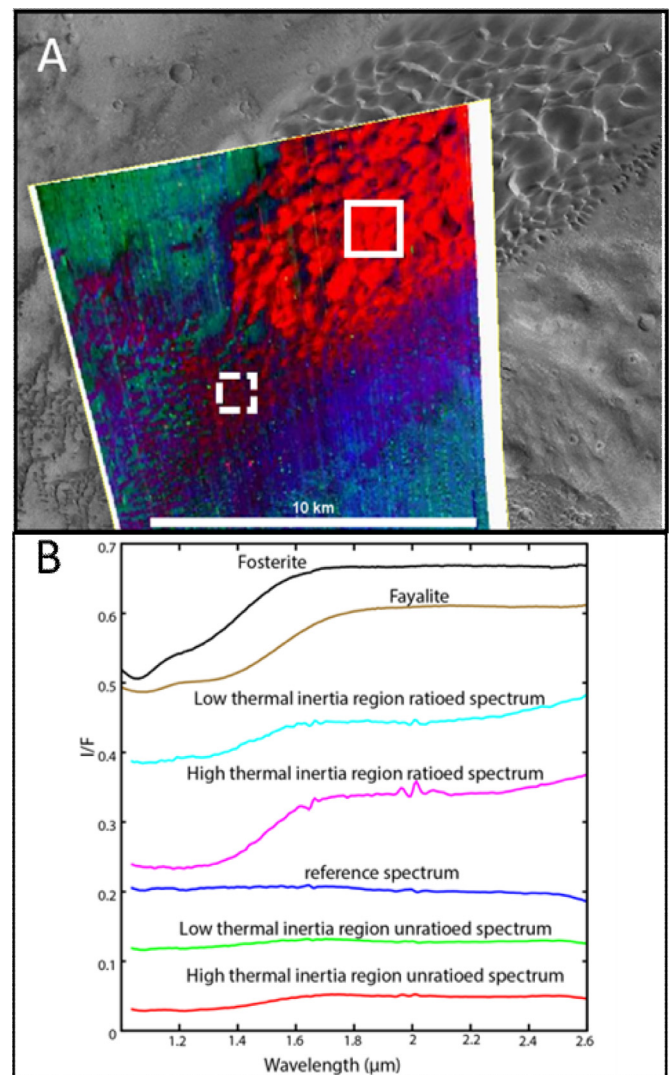


**Fig. 4.** CRISM parameter maps of the dune field within Moreux crater (site D20). A. CRISM mafic index map superposed over CTX images. The colors are as follows: red=OLINDEX (olivine index) with scaling 0.00–0.13, green=LCPINDEX (low Ca pyroxene index) with scaling 0.00–0.1, blue=HCPINDEX (high Ca pyroxene index) with scaling 0.00–0.2. The reference spectrum is within a dusty area outside of the dune field. B. Average spectra of high and low thermal inertia parts of the dune field; both spectra are consistent with an olivine-bearing surface. Laboratory spectra of olivine are plotted for reference. Spectra are offset for clarity. (For interpretation of the references to color in this figure legend, the reader is referred to the web version of this article.)

portions of the highest and lowest thermal inertia areas that are consistent with varying olivine abundance (Fig. 8). However, when spectra are compared with thermal inertia across the entire dune field using thermal inertia intervals (Fig. 9), the relationship between spectral properties and thermal inertia becomes less clear. Indeed, the change of olivine abundance and spectral properties with thermal inertia is very small.

#### 4.2.4. Site D23

Site 23 exhibits thermal inertia values between  $190\text{--}240\text{ J m}^{-2}\text{ s}^{-0.5}\text{ K}^{-1}$  in some areas within the east and west sides of the dune field where dunes are larger (Fig. 2I and J). As with Site 21, there are spectral differences between portions of the high and low thermal inertia areas (Fig. 10), but spectral differences across each thermal inertia interval show limited differences (Fig. 11). Olivine abundances are relatively low compared to Moreux, with little to no relationship to particle size across the entire dune field (Fig. 11).

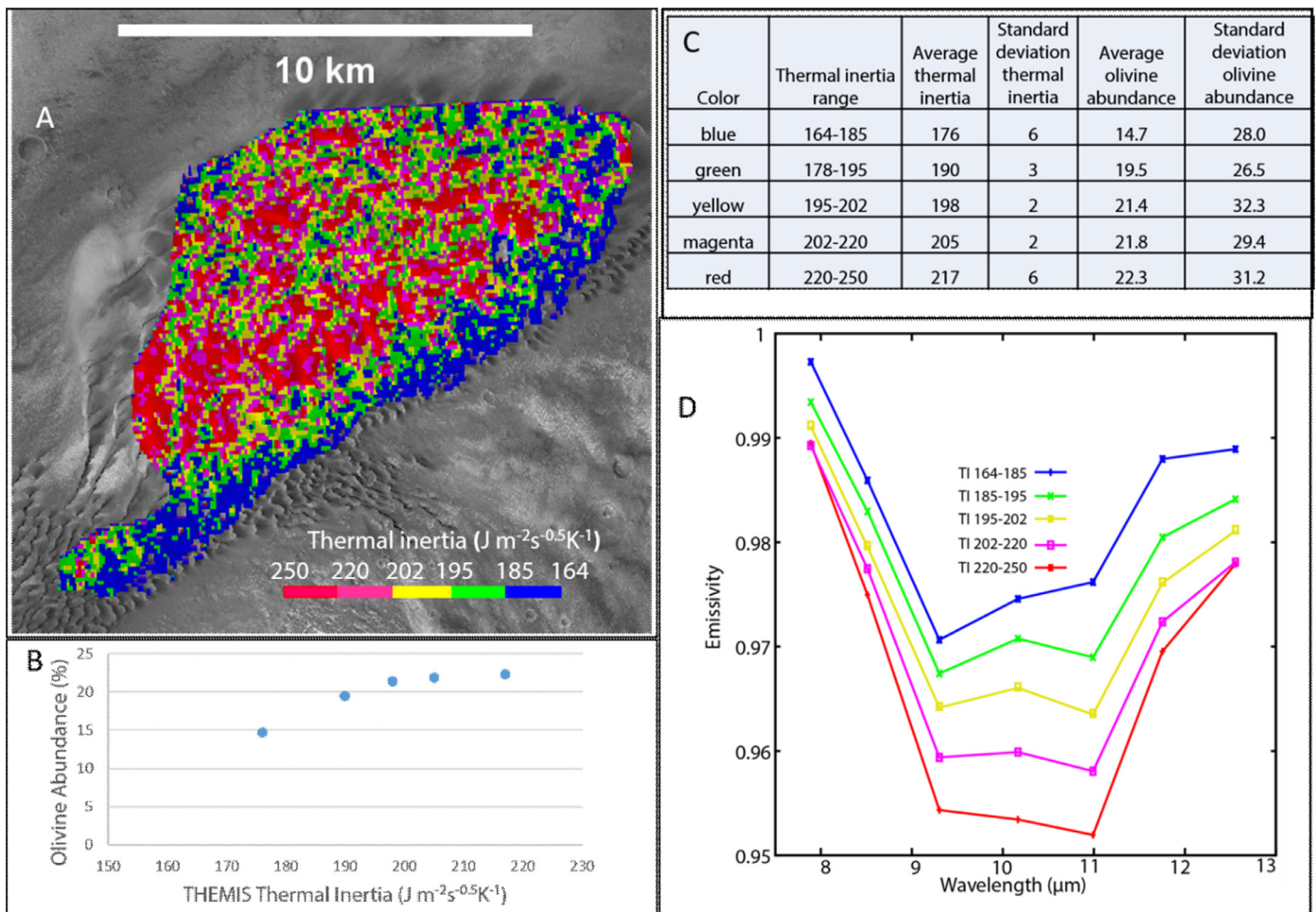


**Fig. 5.** Thermal inertia classification map of the dune field within Moreux crater (site D20), and relationship to olivine abundance. A. Classified THEMIS thermal inertia image superposed over CTX images. Each color represents the 20th percentile of thermal inertia ranges. B. Scatter plot of thermal inertia vs. olivine abundance. C. Mean and standard deviation values of thermal inertia and olivine abundance for each thermal inertia range shown in A. D. Average THEMIS spectra from each thermal inertia (TI) range shown in A. The colors correspond to the class colors in A. Standard deviations about the mean are shown with vertical bars. Spectra are offset for clarity. (For interpretation of the references to color in this figure legend, the reader is referred to the web version of this article.)

From CRISM, reflectance spectra extracted from both the low and high thermal inertia portions of the dune field are consistent with either basaltic glass or a mixture of olivine and orthopyroxene (Fig. 12); however, a major glass component is not consistent with TES spectral data over this site (Supplementary material).

#### 4.3. Analysis of sites D25 and D17

Dune fields at Sites D25 and D17 exhibited spatial continuity in dune field coverage, but little-to-no discernible spectral variability in the THEMIS images. Site D25 is an N-S trending dune field within the western floor of Gale crater that contains a  $\sim 300$  km<sup>2</sup> area of contiguous sand cover (Fig. 13). Immediately to the north of this site, there is a NE-SW trending portion that contains both barchan and linear dune fields (Seelos et al., 2014); this portion of the dune field, informally named the “Bagnold Dunes”, was sampled by the Mars Science Laboratory (MSL) Curiosity Rover. Infrared spectra from this area are consistent with olivine- and pyroxene-bearing basaltic materials (Fig. 13), as reported by previous authors (Lane and Christensen, 2013; Lapotre et al., 2015; Rogers and Bandfield, 2009; Seelos et al., 2014). The Bagnold dune portion of this sedimentary deposit was not examined for compositional – particle size relationships due to significant interdune surfaces present. However, compositional variability was previously observed over a portion of this region at smaller scales using

CRISM data (Seelos et al., 2014) (Section 2). Site D25 exhibits color variations in the THEMIS DCS images (using bands 8–7–5 as red–green–blue), ranging from orange to pink. However, spectral averages from these different colored areas show that the spectral differences are very minor, particularly compared to other dune fields investigated within Moreux crater and site D1 (Fig. 13). It is possible that the spectral uniformity is due to obscuration by a thin dust cover, consistent with TES albedo and DCI values over this site.

Site D17 (Hargraves crater) exhibits contiguous sediment coverage, with thermal inertia values ranging between 202–296 J m<sup>-2</sup> s<sup>-0.5</sup> K<sup>-1</sup>. Unlike most of the other dune fields examined, the spatial variation in thermal inertia does not appear to be related to changes in morphology, and there is no clear pattern of distribution (Fig. 2E and F). No spectral variability was observed in THEMIS DCS images over this site.

## 5. Discussion

Of the 25 sites examined, only four exhibited clear spatial heterogeneity in compositional characteristics in THEMIS imagery. The rarity of compositional heterogeneity within dune fields in our study region can be attributed to one or more factors; we describe four possibilities below, and consider the first two to be the most likely. First, drawing from the experimental results of

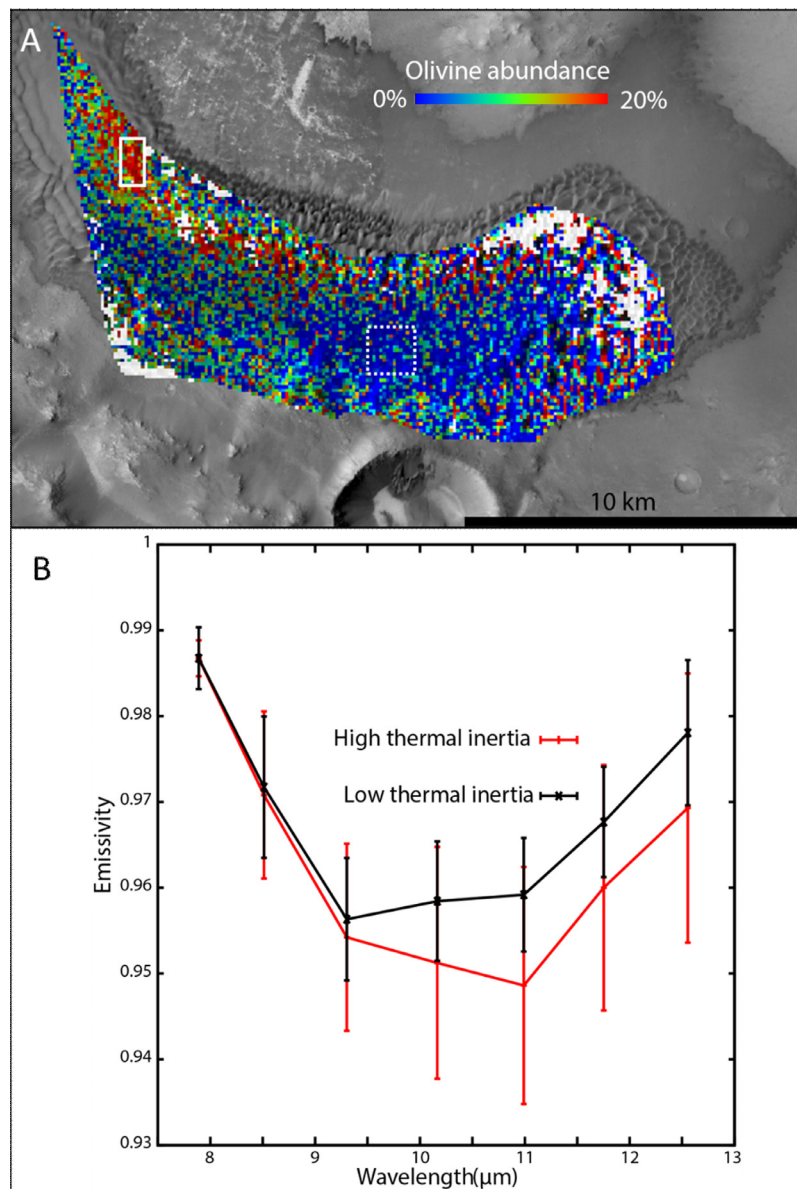


**Fig. 6.** THEMIS compositional data for dune field D1. A. THEMIS derived olivine abundance superposed over CTX images. White polygons indicate locations of spectral extraction in B; solid=high thermal inertia region, dashed=low thermal inertia region. B. Average THEMIS emissivity spectra from high and low thermal inertia parts of the dune field.

Fedo et al. (2015) (Section 2), the source protoliths for many of the dune fields could have been phenocryst-poor, resulting in derived sediments that are dominated by sand-sized lithic or glass fragments rather than individual mineral grains. Clear evidence for significant glass was not observed in the dune fields examined, which could suggest that if the sands are phenocryst poor, they are likely dominated by lithic fragments rather than glass. However, Fe-bearing glasses can be difficult to detect when mixed with other minerals such as olivine and pyroxene (Horgan et al., 2014). Sediments characterized by X-ray diffraction with the Mars Science Laboratory CheMin instrument, at the “Rocknest” sediment patch target in Gale crater, contain ~30–45 wt% X-ray amorphous materials, of which volcanic glass is a plausible dominant component (e.g. Dehouck et al., 2014). In addition, recent models of thermal infrared spectra from many sand-covered Martian regions using newly-acquired laboratory spectra of terrestrial hydrovolcanic samples incorporate significant abundances of devitrified basaltic glass (Farrand et al., 2016), and basaltic glass has also been detected in

other dune fields from near-infrared data (Horgan and Bell, 2012; Chojnacki et al., 2014a,b). Thus the possibility of glassy sediments elsewhere on Mars is within reason.

Second, it is possible that the dune fields are heterogeneous at spatial scales below the resolution of the THEMIS images (< 100 m/pixel), but not at larger spatial scales. Examples of smaller scale variation, such as at the scale of individual bedforms, have been shown previously using in-situ or CRISM data (Sullivan et al., 2008; Chojnacki et al., 2014a,b; Seelos et al., 2014). This would suggest that sorting only produces compositional changes across smaller scales, and that compositional variability observed between sediment fields or other surface units is more related to spatial variations in sand source protolith compositions.

A third possibility is that the particle size ranges within some of these dune fields may be narrow enough such that very little sorting and separation can occur. However, spatial sorting does not necessarily require a wide particle size range. For example, the particle size range of Moreux crater is 63–226 μm, corresponding to

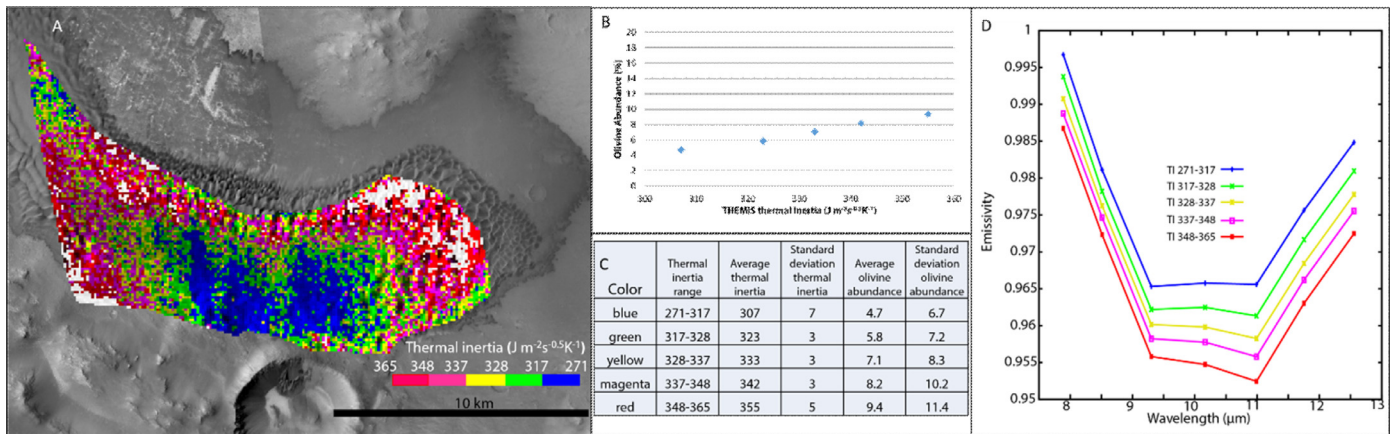


**Fig. 7.** Thermal inertia classification map of dune field D1. A. Classified THEMIS thermal inertia image superposed over CTX images. Each color represents the 20th percentile of thermal inertia ranges. B. Scatter plot of thermal inertia vs. olivine abundance. C. Mean and standard deviation values of thermal inertia and olivine abundance for each thermal inertia (TI) range shown in A. D. Average THEMIS spectra from each thermal inertia range shown in A. The colors correspond to the class colors in A. Standard deviations about the mean are shown with vertical bars. Spectra are offset for clarity. (For interpretation of the references to color in this figure legend, the reader is referred to the web version of this article.)

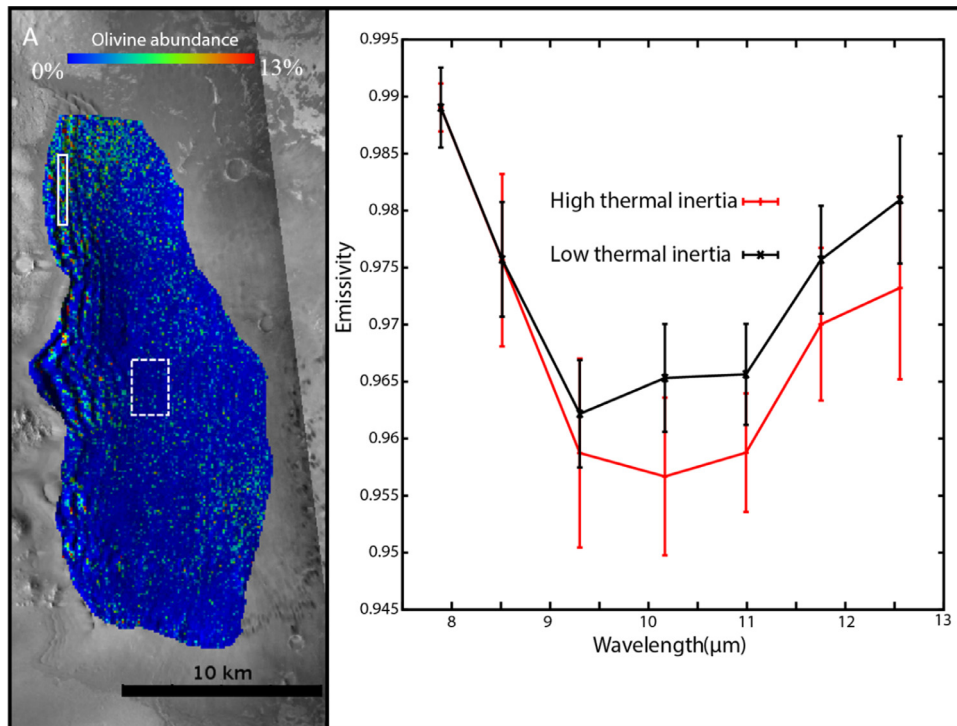


**Fig. 8.** THEMIS compositional data for dune field D21. A. THEMIS derived olivine abundance map superposed over CTX images. White polygons indicate locations of spectral extraction in B; solid=high thermal inertia region, dashed=low thermal inertia region. B. Average THEMIS spectra from high and low thermal inertia parts of the dune field.

very fine to fine sand, yet significant spatial variability within the dune field is observed.

Last, grain populations consisting of individual minerals may have been compositionally homogenized across size fractions through multiple meteor impacts. We consider this to be less likely due to impact comminution experiments that show that repeated impacts lead to mineral-specific comminution (Horz et al., 1984).

Among the four spectrally heterogeneous dune fields, two (within Moreux crater and D1) show a strong positive relationship between olivine and particle size, similar to smaller-scale trends described for Gale crater (Lapotre et al., 2015) and the El Dorado ripple field (Sullivan et al., 2008), but notably, opposite the trend described for basaltic sediments in Iceland (Mangold et al., 2011). The portions of these two dune fields with larger effective particle

size exhibit higher olivine abundance and distinct bedforms, whereas regions with smaller effective particle size are relatively olivine poor. For the remaining two dune fields (D21 and D23), spectral variation is observed, but the relationship to thermal inertia is less clear. Broad averages of spectral emissivity across select high- and low-thermal inertia portions of the dune field suggest that some compositional sorting may have occurred (Figs. 9–11). However, there is great overlap in the olivine abundances within each thermal inertia range for these two dune fields, indicating that the relationship between thermal inertia and composition is imperfect and suggesting that spatial compositional sorting is less well-developed. The few areas of elevated olivine abundance could be due to local inputs from areally minor olivine-rich bedrock. Other possible causes could relate to complicating factors in

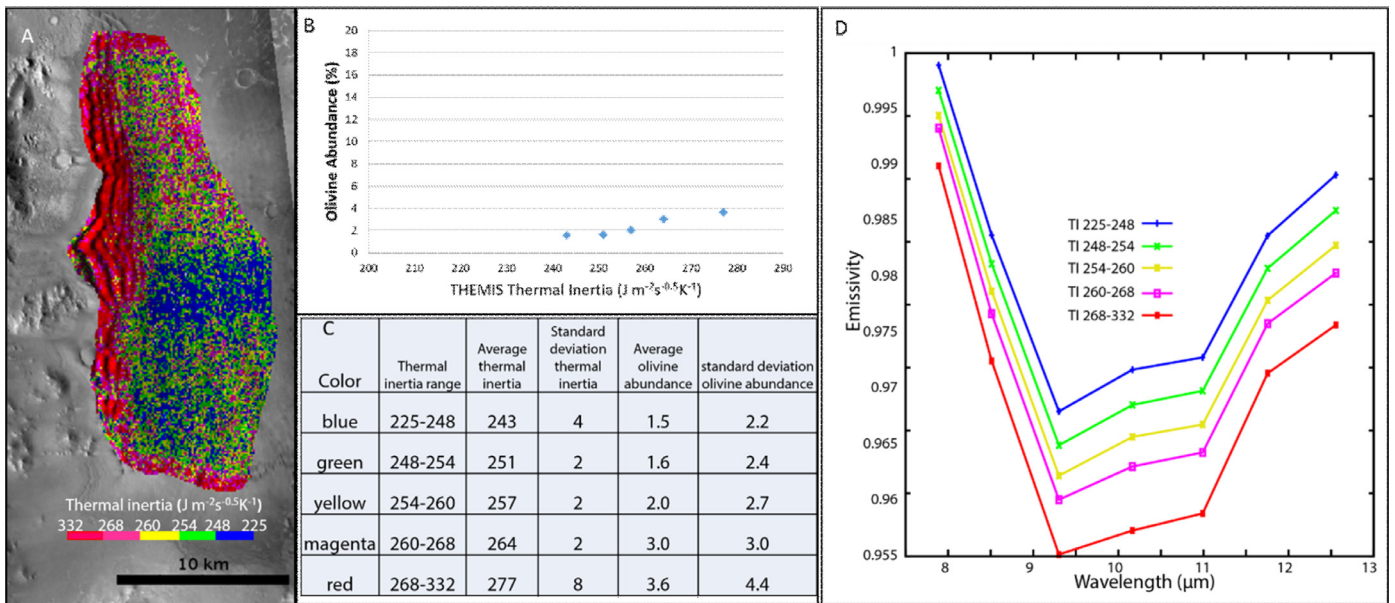


**Fig. 9.** Thermal inertia classification map of dune field D21. A. Classified THEMIS thermal inertia image superposed over CTX images. Each color represents the 20th percentile of thermal inertia ranges. B. Scatter plot of thermal inertia vs. olivine abundance. C. Mean and standard deviation values of thermal inertia (TI) and olivine abundance for each thermal inertia range shown in A. D. Average THEMIS spectra from each thermal inertia range shown in A. The colors correspond to the class colors in A. Standard deviations about the mean are shown with vertical bars. Spectra are offset for clarity. (For interpretation of the references to color in this figure legend, the reader is referred to the web version of this article.)

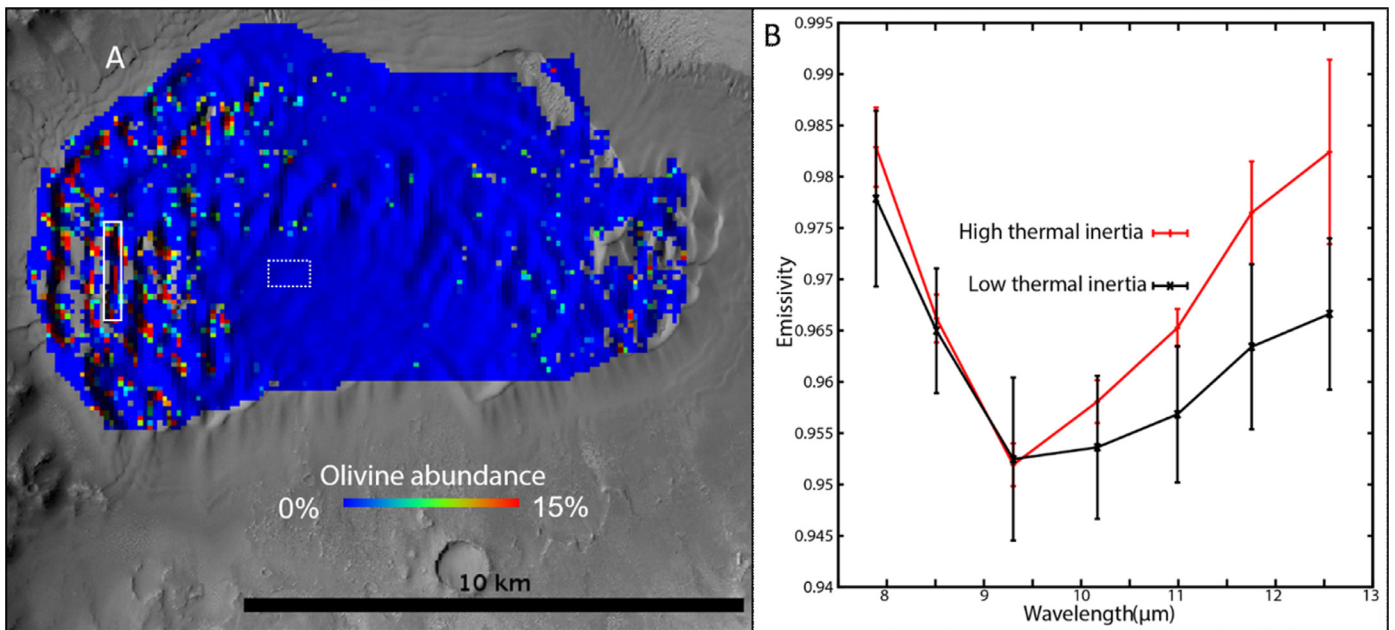


**Fig. 10.** THEMIS-derived olivine abundance map of dune field D23. A. THEMIS derived olivine abundance superposed over CTX images. White polygons indicate locations of spectral extraction in B; solid=high thermal inertia region, dashed=low thermal inertia region. B. Average spectra of high and low thermal inertia parts of the dune field.

deriving thermal inertia (e.g. not accounting for slope/aspect angles) or to slight misregistration of daytime and nighttime THEMIS images (Section 3).

From the available data, it is difficult to determine whether the sediments in the spectrally heterogeneous dune fields are from a single source that contains large olivine phenocrysts within a finely crystalline matrix, or from multiple sources. In any case, this study highlights the fact that relationships between aeolian sediment compositions and particle sizes cannot be easily predicted on Mars using terrestrial examples, without knowledge of the source rock petrographic textures and compositions (e.g. Fedo et al., 2015).

## 6. Conclusion

We investigated 25 dune fields and sand deposits within impact craters located between (45°N, 5°E) and (20°S, 185°E), to assess the degree and occurrence of thermophysical and compositional heterogeneity. Of these 25 sites, only four dune fields exhibit spatial heterogeneity in spectral properties and composition. Nearly all exhibit spatial heterogeneity in thermophysical properties, but, for all but six sites, it is difficult to rule out interdune/non-sand surfaces as the dominant source of that thermophysical heterogeneity.

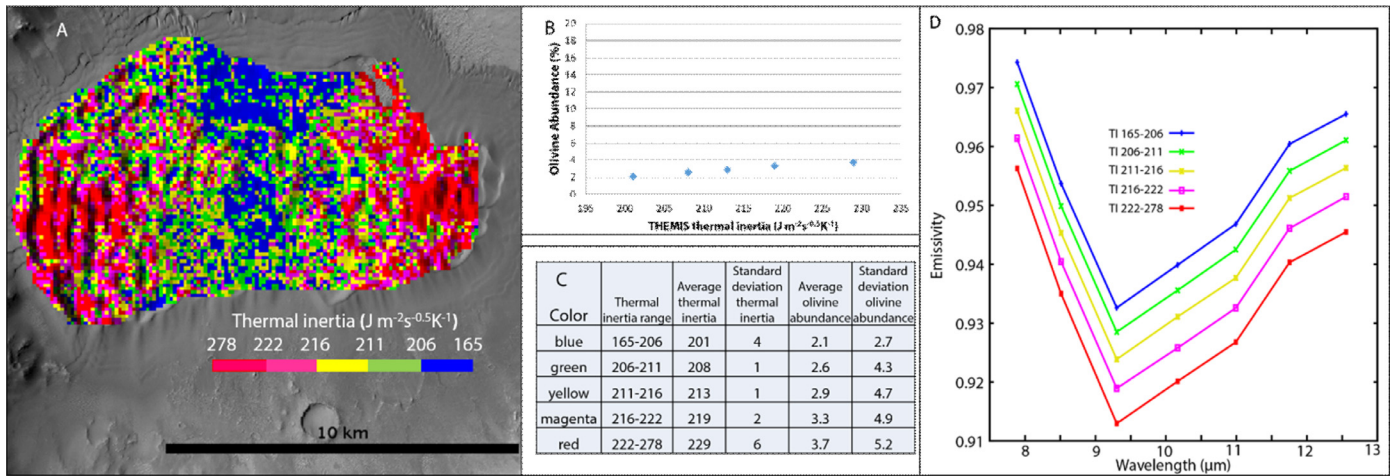


**Fig. 11.** Thermal inertia classification map of dune field D23. A. Classified THEMIS thermal inertia image superposed over CTX images. Each color represents the 20th percentile of thermal inertia ranges. B. Scatter plot of thermal inertia vs. olivine abundance. C. Mean and standard deviation values of thermal inertia and olivine abundance for each thermal inertia range shown in A. D. Average THEMIS spectra from each thermal inertia (TI) range shown in A. The colors correspond to the class colors in A. Standard deviations about the mean are shown with vertical bars. Spectra are offset for clarity. (For interpretation of the references to color in this figure legend, the reader is referred to the web version of this article.)

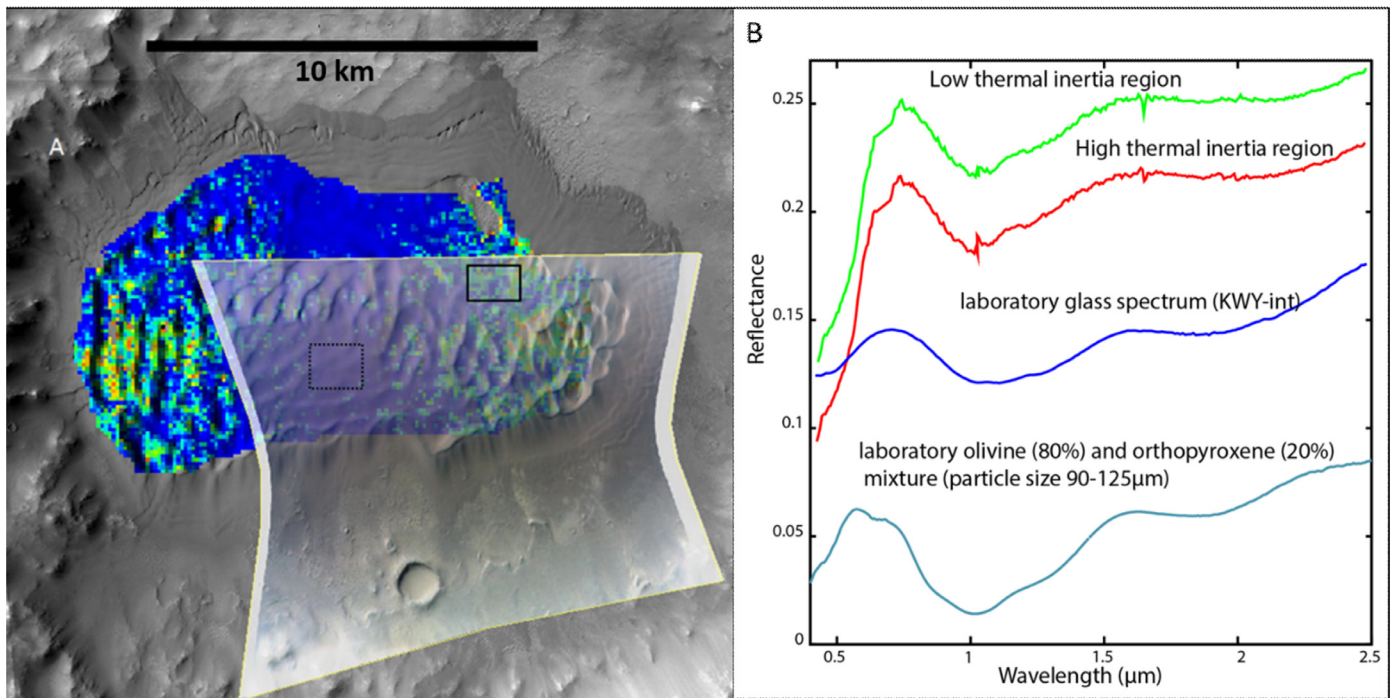


**Fig. 12.** CRISM spectra of dune field D23. A. CRISM enhanced visible color image overlain on THEMIS thermal inertia and CTX showing the coverage of the CRISM image. Black polygons indicate locations of spectral extraction in B; solid=high thermal inertia region, dashed=low thermal inertia region. B. CRISM unratiod spectra from a high and low thermal inertia region, compared with laboratory spectra of glass from (Minitti et al., 2007) and a mixture of olivine and orthopyroxene (Horgan et al., 2014). Spectra are offset for clarity. (For interpretation of the references to color in this figure legend, the reader is referred to the web version of this article.)

The rarity of well-developed spatial compositional sorting within dune fields in our study region could be due to one or more factors, but is most likely related to composition and texture of the individual sediment source rocks or the spatial resolution of the thermal infrared data (100 m/pixel) used to search for spatial heterogeneity. Phenocryst-poor source materials, such as volcaniclastic/glassy lithologies or finely crystalline basalts would not be expected to exhibit strong compositional relationships with particle size. Alternatively, heterogeneity could be present at the individual bedform scale, but not at the scale of the whole dune field (~10–20 km) (Section 5). These results suggest that aeolian transport and hydrodynamic sorting are unlikely to be sole factors in caus-

ing significant compositional variability observed in Martian surface materials at ~10 km or larger scales.

Two dune fields in our study region show a strong positive relationship between particle size and olivine abundance. This relationship is similar to observations of the “El Dorado” ripple field, which was investigated by the Mars Exploration Rover *Spirit* (Sullivan et al., 2008), Valles Marineris dunes (Chojnacki et al., 2014b), and the Bagnold dune field in Gale crater (Seelos et al., 2014). However, this trend is opposite of what was observed by Mangold et al. (2011) for basaltic sediments on Earth. These differing trends suggest that composition and particle size relationships observed in terrestrial basaltic settings cannot be extrapolated to

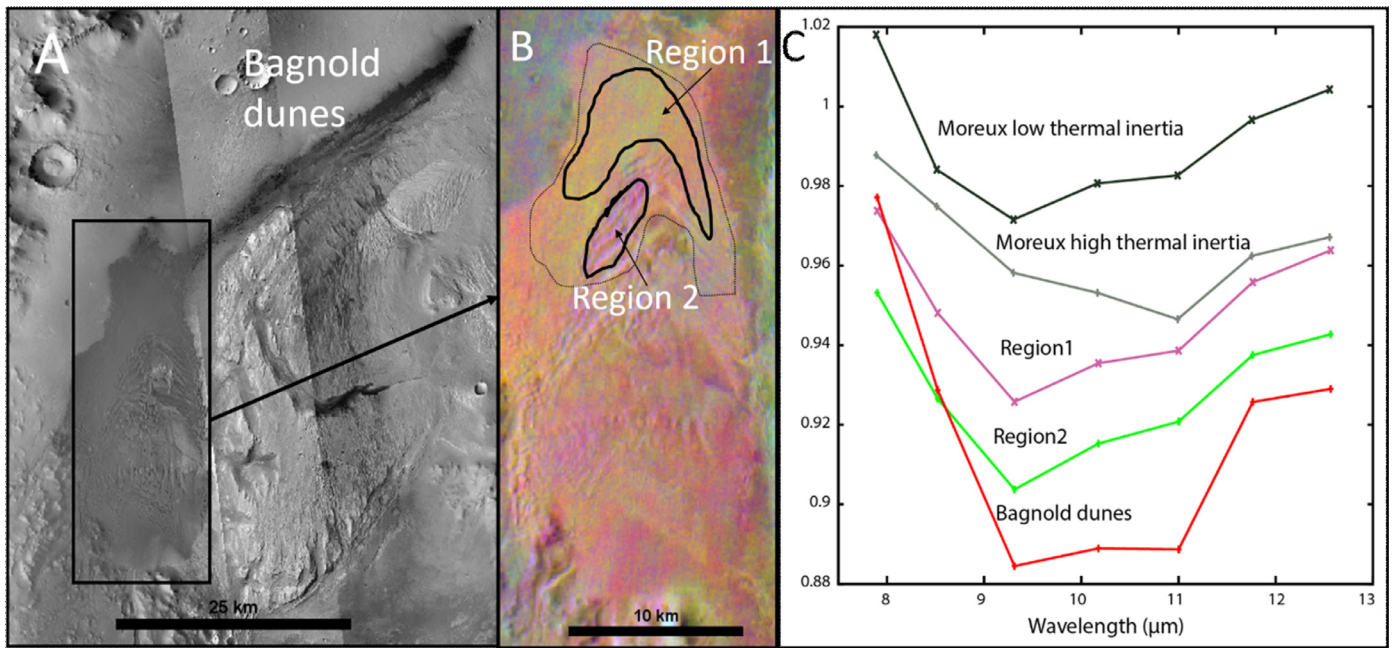


**Fig. 13.** THEMIS analysis of dune sediments at Site D25, located south of the “Bagnold” dunes in Gale crater (Site D25). A. CTX mosaic of dark sediments on the western floor of Gale crater. Black polygon indicates area shown in B. B. THEMIS bands 8 (~11.8  $\mu\text{m}$ )–7 (~11  $\mu\text{m}$ )–5 (~9.4  $\mu\text{m}$ ) as red-green-blue in the DCS radiance mosaic. Dashed polygon shows boundary of Site D25. Solid line polygons show two regions with color variation in DCS image that are suggestive of compositional variation; average spectra from these regions are shown in C. C. THEMIS spectra from regions 1 and 2. Despite color differences in the DCS image, little spectral difference is present between these two regions. For comparison, THEMIS spectra from the Bagnold dunes, as well as from low and high thermal inertia areas within the Moreux dune field are also shown. Spectra are offset for clarity. (For interpretation of the references to color in this figure legend, the reader is referred to the web version of this article.)

Mars in any simple manner and is dependent on source material texture and composition.

### Acknowledgments

We thank Matt Chojnacki and an anonymous reviewer for thorough, insightful reviews that greatly improved this manuscript. We thank Scott McLennan for an informal review of an early version of this manuscript. A. D. R. acknowledges funding from the Mars Odyssey Project and C. Pan acknowledges funding from the NASA Earth and Space Science Fellowship program. The JMARS and Davinci software and CRISM Analysis Toolkit programs, produced by Arizona State University and Johns Hopkins Applied Physics Laboratory, respectively, greatly enhanced the ease in which this project could be completed; we thank the persons responsible for these products.

### Supplementary materials

Supplementary material associated with this article can be found, in the online version, at [doi:10.1016/j.icarus.2016.09.021](https://doi.org/10.1016/j.icarus.2016.09.021).

### References

- Anderson, R.S., Bunas, K.L., 1993. Grain-size segregation and stratigraphy in aeolian ripples modeled with a cellular-automation. *Nature* 365, 740–743. doi:[10.1038/365740a0](https://doi.org/10.1038/365740a0).
- Bandfield, J.L., Edgett, K.S., Christensen, P.R., 2002. Spectroscopic study of the Moses lake dune field, Washington: determination of compositional distributions and source lithologies. *J. Geophys. Res.-Planets* 107. doi:[10.1029/2000je001469](https://doi.org/10.1029/2000je001469).
- Bandfield, J.L., Rogers, D., Smith, M.D., Christensen, P.R., 2004. Atmospheric correction and surface spectral unit mapping using thermal emission imaging system data. *J. Geophys. Res.-Planets* 109 doi:[E1000810.1029/2004je002289](https://doi.org/10.1029/2004je002289).
- Bibring, J.-P., et al., 2004. OMEGA: Observatoire pour la Minéralogie, l’Eau, les Glaces et l’Activité. In: Wilson, A., Chicarro, A. (Eds.), *Mars Express: The Scientific Payload*, 1240. ESA Special Publication, Noordwijk, The Netherlands, pp. 37–49.
- Blake, D.F., et al., 2013. Curiosity at Gale Crater, Mars: characterization and analysis of the rocknest sand shadow. *Science* 341. doi:[10.1126/science.1239505](https://doi.org/10.1126/science.1239505).
- Boggs, S., 2006. *Principles of Sedimentology and Stratigraphy*. Pearson Prentice Hall.

- Chojnacki, M., Burr, D.M., Moersch, J.E., 2014a. Valles marineris dune fields as compared with other martian populations: diversity of dune compositions, morphologies, and thermophysical properties. *Icarus* 230, 96–142. doi:[10.1016/j.icarus.2013.08.018](https://doi.org/10.1016/j.icarus.2013.08.018).
- Chojnacki, M., Burr, D.M., Moersch, J.E., Michaels, T.I., 2011. Orbital observations of contemporary dune activity in endeavor crater, meridiani Planum, Mars. *J. Geophys. Res.-Planets* 116. doi:[10.1029/2010je003675](https://doi.org/10.1029/2010je003675).
- Chojnacki, M., Burr, D.M., Moersch, J.E., Wray, J.J., 2014b. Valles marineris dune sediment provenance and pathways. *Icarus* 232, 187–219. doi:[10.1016/j.icarus.2014.01.011](https://doi.org/10.1016/j.icarus.2014.01.011).
- Christensen, P.R., et al., 2001. Mars global surveyor thermal emission spectrometer experiment: investigation description and surface science results. *J. Geophys. Res.-Planets* 106, 23823–23871. doi:[10.1029/2000je001370](https://doi.org/10.1029/2000je001370).
- Christensen, P.R., Fergason, R.L., Edwards, C.S., Hill, J., 2013. THEMIS-derived thermal inertia mosaic of Mars: product description and science results. *Lunar and Planetary Science Conference 44*, 2822.
- Christensen, P.R., et al., 2004. The thermal emission imaging system (THEMIS) for the Mars 2001 Odyssey mission. *Space Sci Rev* 110, 85–130. doi:[10.1023/b:spac.0000021008.16305.94](https://doi.org/10.1023/b:spac.0000021008.16305.94).
- Dehouck, E., McLennan, S.M., Meslin, P.Y., Cousin, A., 2014. Constraints on abundance, composition, and nature of X-ray amorphous components of soils and rocks at Gale crater, Mars. *J. Geophys. Res.-Planets* 119, 2640–2657. doi:[10.1002/2014je004716](https://doi.org/10.1002/2014je004716).
- Edgett, K.S., Christensen, P.R., 1994. Mars aeolian sand - regional variations among dark-hued crater floor features. *J. Geophys. Res.-Planet.* 99, 1997–2018. doi:[10.1029/93je03094](https://doi.org/10.1029/93je03094).
- Edgett, K.S., Christensen, P.R., 1991. The Particle-size of martian aeolian dunes. *J. Geophys. Res.-Planets* 96, 22765–22776. doi:[10.1029/91je02412](https://doi.org/10.1029/91je02412).
- Edgett, K.S., Lancaster, N., 1993. Volcaniclastic aeolian dunes-terrestrial examples and application to martian sands. *Journal of Arid Environments*. 25, 271–297. doi:[10.1006/jare.1993.1061](https://doi.org/10.1006/jare.1993.1061).
- Edwards, C.S., Bandfield, J.L., Christensen, P.R., Fergason, R.L., 2009. Global distribution of bedrock exposures on Mars using THEMIS high-resolution thermal inertia. *J. Geophys. Res.-Planets* 114. doi:[10.1029/2009je003363](https://doi.org/10.1029/2009je003363).
- Edwards, C.S., Bandfield, J.L., Christensen, P.R., Rogers, A.D., 2014. The formation of infilled craters on Mars: evidence for widespread impact induced decompression of the early martian mantle. *Icarus* 228, 149–166. doi:[10.1016/j.icarus.2013.10.005](https://doi.org/10.1016/j.icarus.2013.10.005).
- Farrand, W.H., Wright, S.P., Rogers, A.D., Glotch, T.D., 2016. Basaltic glass formed from hydrovolcanism and impact processes: Characterization and clues for detection of mode of origin from VNIR through MWIR reflectance and emission spectroscopy. *Icarus* 275, 16–28. doi:[10.1016/j.icarus.2016.03.027](https://doi.org/10.1016/j.icarus.2016.03.027).
- Fedo, C.M., McGlynn, I.O., McSween, H.Y., 2015. Grain size and hydrodynamic sorting controls on the composition of basaltic sediments: implications for interpreting Martian soils. *Earth Planet. Sci. Lett.* 423, 67–77. doi:[10.1016/j.epsl.2015.03.052](https://doi.org/10.1016/j.epsl.2015.03.052).

- Fenton, L.K., Mellon, M.T., 2006. Thermal properties of sand from thermal emission spectrometer (TES) and thermal emission imaging system (THEMIS): spatial variations within the proctor crater dune field on mars. *J. Geophys. Res.-Planets* 111. doi:[10.1029/2004je002363](https://doi.org/10.1029/2004je002363).
- Ferguson, R.L., Christensen, P.R., Bell, J.F., Golombek, M.P., Herkenhoff, K.E., Kieffer, H.H., 2006. Physical properties of the mars exploration rover landing sites as inferred from Mini-TES-derived thermal inertia. *J. Geophys. Res.-Planets* 111. doi:[10.1029/2005je002583](https://doi.org/10.1029/2005je002583).
- Gillespie, A.R., Kahle, A.B., Walker, R.E., 1986. Color enhancement of highly correlated images. 1. Decorrelate and HSI contrast stretches. *Remote Sens. Environ.* 20, 209–235. doi:[10.1016/0034-4257\(86\)90044-1](https://doi.org/10.1016/0034-4257(86)90044-1).
- Greeley, R., Peterfreund, A.R., 1981. Aeolian “megaripples” examples from mono Craters, California and northern iceland [abs]. *Geological Society of America, Abstracts with Programs* 13, 463.
- Hamilton, V.E., Christensen, P.R., 2005. Evidence for extensive, olivine-rich bedrock on mars. *Geology*, 33, 433–436. doi:[10.1130/g21258.1](https://doi.org/10.1130/g21258.1).
- Hamilton, V.E., Christensen, P.R., McSween, H.Y., 1997. Determination of Martian meteorite lithologies and mineralogies using vibrational spectroscopy. *J. Geophys. Res.-Planet.* 102, 25593–25603. doi:[10.1029/97je01874](https://doi.org/10.1029/97je01874).
- Hapke, B.W., 1993. *Theory of Reflectance and Emittance Spectroscopy*. Cambridge University Press, Cambridge, U.K.
- Hayward, R.K., Fenton, L.K., Titus, T.N., 2014. Mars global digital dune database (MGD(3)): global dune distribution and wind pattern observations. *Icarus* 230, 38–46. doi:[10.1016/j.icarus.2013.04.011](https://doi.org/10.1016/j.icarus.2013.04.011).
- Horgan, B., Bell III, J.F., 2012. Widespread weathered glass on the surface of Mars. *Geology*, 40, 391–394. doi:[10.1130/g32755.1](https://doi.org/10.1130/g32755.1).
- Horgan, B., Cloutis, E.A., Mann, P., Bell, J.F., 2014. Near-infrared spectra of ferrous mineral mixtures and methods for their identification in planetary surface spectra. *Icarus* 234, 132–154. doi:[10.1016/j.icarus.2014.02.031](https://doi.org/10.1016/j.icarus.2014.02.031).
- Horz, F., Cintala, M.J., See, T.H., Cardenas, F., Thompson, T.D., 1984. Grain-size evolution and fractionation trends in an experimental regolith. *J. Geophys. Res.* 89, C183–C196. doi:[10.1029/JB089iS01p0C183](https://doi.org/10.1029/JB089iS01p0C183).
- Jakosky, B.M., 1979. Effects of nonideal surfaces on the derived thermal-properties of mars. *J. Geophys. Res.* 84, 8252–8262. doi:[10.1029/JB084iB14p08252](https://doi.org/10.1029/JB084iB14p08252).
- Karunatillake, S., McLennan, S., Herkenhoff, K.E., 2010. Regional and grain size influences on the geochemistry of soil at Gusev Crater, Mars. *J. Geophys. Res.-Planets* 115. doi:[10.1029/2010je003637](https://doi.org/10.1029/2010je003637).
- Kieffer, H.H., Martin, T., Peterfreund, A.R., Jakosky, B.M., Miner, E.D., Palluconi, F.D., 1977. Thermal and albedo mapping of mars during the viking primary mission. *J. Geophys. Res.* 82, 4249–4291. doi:[10.1029/JS082i028p0424](https://doi.org/10.1029/JS082i028p0424).
- Kieffer, H.H., Chase, S.C., Miner, E., Munch, G., Neugebauer, G., 1973. Preliminary report on infrared radiometric measurements from mariner-9 spacecraft. *J. Geophys. Res.* 78, 4291–4312. doi:[10.1029/JB078i020p04291](https://doi.org/10.1029/JB078i020p04291).
- Kiminami, K., Fujii, K., 2007. The relationship between major element concentration and grain size within sandstones from four turbidite sequences in japan. *Sediment. Geol.* 195, 203–215. doi:[10.1016/j.sedgeo.2006.08.002](https://doi.org/10.1016/j.sedgeo.2006.08.002).
- Lane, M.D., Christensen, P.R., 2013. Determining olivine composition of basaltic dunes in Gale Crater, Mars, from orbit: awaiting ground truth from curiosity. *Geophys. Res. Lett.* 40, 3517–3521. doi:[10.1002/grl.50621](https://doi.org/10.1002/grl.50621).
- Lapotre, M., et al., 2015. The bagnold dunes at gale Crater—a key to reading the geologic record of mount sharp. *Lunar Planet. Sci. Conf.* 46, 1634.
- Makse, H.A., 2000. Grain segregation mechanism in aeolian sand ripples. *Eur. Phys. J. E*, 1, 127–135. doi:[10.1007/pl00014592](https://doi.org/10.1007/pl00014592).
- Malin, M.C., et al., 2007. Context camera investigation on board the Mars reconnaissance orbiter. *J. Geophys. Res.-Planets* 112, 25. doi:[10.1029/2006je002808](https://doi.org/10.1029/2006je002808).
- Mangold, N., et al., 2011. Segregation of olivine grains in volcanic sands in Iceland and implications for Mars. *Earth Planet. Sci. Lett.* 310, 233–243. doi:[10.1016/j.epsl.2011.07.025](https://doi.org/10.1016/j.epsl.2011.07.025).
- McDowell, M.L., Hamilton, V.E., 2007. Geologic characteristics of relatively high thermal inertia intracrater deposits in southwestern margaritifer Terra, Mars. *J. Geophys. Res.-Planets* 112. doi:[10.1029/2007je002925](https://doi.org/10.1029/2007je002925).
- McGlynn, I.O., Fedo, C.M., McSween, H.Y., 2011. Origin of basaltic soils at gusev crater, Mars, by aeolian modification of impact-generated sediment. *J. Geophys. Res.-Planets* 116, 15. doi:[10.1029/2010je003712](https://doi.org/10.1029/2010je003712).
- McGuire, P.C., et al., 2009. An improvement to the volcano-scan algorithm for atmospheric correction of CRISM and OMEGA spectral data. *Planet. Space Sci.* 57, 809–815. doi:[10.1016/j.pss.2009.03.007](https://doi.org/10.1016/j.pss.2009.03.007).
- Minitti, M.E., Weitz, C.M., Lane, M.D., Bishop, J.L., 2007. Morphology, chemistry, and spectral properties of hawaiian rock coatings and implications for mars. *J. Geophys. Res.-Planets* 112, 24. doi:[10.1029/2006je002839](https://doi.org/10.1029/2006je002839).
- Moore, H.J., Hutton, R., Clow, G., Spitzer, C., 1987. Physical properties of the surface materials at the Viking landing sites on Mars.
- Moore, H.J., et al., 1999. Soil-like deposits observed by Sojourner, the pathfinder rover. *J. Geophys. Res.-Planets* 104, 8729–8746. doi:[10.1029/1998je900005](https://doi.org/10.1029/1998je900005).
- Murchie, S.L., et al., 2007. Compact reconnaissance imaging spectrometer for mars (CRISM) on Mars reconnaissance orbiter (MRO). *J. Geophys. Res.-Planets* 112, E05s03. doi:[10.1029/2006je002682](https://doi.org/10.1029/2006je002682).
- Ody, A., et al., 2012. Global maps of anhydrous minerals at the surface of Mars from OMEGA/MEX. *J. Geophys. Res.-Planets* 117. doi:[10.1029/2012je004117](https://doi.org/10.1029/2012je004117).
- Pan, C., Rogers, A.D., Michalski, J.R., 2015. Thermal and near-infrared analyses of central peaks of Martian impact craters: evidence for a heterogeneous martian crust. *J. Geophys. Res.-Planets* 120, 662–688. doi:[10.1002/2014je004676](https://doi.org/10.1002/2014je004676).
- Pettijohn, F.J., Potter, P.E., Siever, R., 1987. *Sand and Sandstone*. Springer Science & Business Media, New York, US.
- Presley, M.A., Christensen, P.R., 1997. Thermal conductivity measurements of particulate materials 0.2. Results. *J. Geophys. Res.-Planets* 102, 6551–6566. doi:[10.1029/96je03303](https://doi.org/10.1029/96je03303).
- Rogers, A.D., Bandfield, J.L., 2009. Mineralogical characterization of Mars science laboratory candidate landing sites from THEMIS and TES data. *Icarus* 203, 437–453. doi:[10.1016/j.icarus.2009.04.020](https://doi.org/10.1016/j.icarus.2009.04.020).
- Rogers, A.D., Christensen, P.R., 2007. Surface mineralogy of Martian low-albedo regions from MGS-TES data: implications for upper crustal evolution and surface alteration. *J. Geophys. Res.-Planets* 112. doi:[10.1029/2006je002727](https://doi.org/10.1029/2006je002727).
- Rogers, A.D., Hamilton, V.E., 2015. Compositional provinces of mars from statistical analyses of TES, GRS, OMEGA and CRISM data. *J. Geophys. Res.-Planets* 120, 62–91. doi:[10.1002/2014je004690](https://doi.org/10.1002/2014je004690).
- Ruff, S.W., Christensen, P.R., 2002. Bright and dark regions on Mars: particle size and mineralogical characteristics based on thermal emission spectrometer data. *J. Geophys. Res.-Planets* 107, 22. doi:[10.1029/2001je001580](https://doi.org/10.1029/2001je001580).
- Salisbury, J.W., 1993. Mid-infrared spectroscopy laboratory data. In: Pieters, C.M., Englert, P.A. (Eds.), *Remote Geochemical Analysis: Elemental and Mineralogical Composition*. Cambridge University Press, Cambridge, U.K., pp. 79–98.
- Seelos, K.D., et al., 2014. Mineralogy of the MSL curiosity landing site in Gale Crater as observed by MRO/CRISM. *Geophys. Res. Lett.* 41, 4880–4887. doi:[10.1002/2014gl060310](https://doi.org/10.1002/2014gl060310).
- Sullivan, R., et al., 2008. Wind-driven particle mobility on Mars: insights from mars exploration rover observations at “El Dorado” and surroundings at gusev crater. *J. Geophys. Res.-Planets* 113. doi:[10.1029/2008je003101](https://doi.org/10.1029/2008je003101).
- Taylor, G.J., Boynton, W.V., McLennan, S.M., Martel, L.M.V., 2010. K and Cl concentrations on the martian surface determined by the mars odyssey gamma ray Spectrometer: implications for bulk halogen abundances in mars. *Geophys. Res. Lett.* 37. doi:[10.1029/2010gl043528](https://doi.org/10.1029/2010gl043528).
- Taylor, S.R., McLennan, S., 2009. *Planetary Crusts: Their Composition, Origin and Evolution*. Cambridge University Press.
- Tirsch, D., Jaumann, R., Pacifici, A., Poulet, F., 2011. Dark aeolian sediments in martian craters: composition and sources. *J. Geophys. Res.-Planets* 116. doi:[10.1029/2009je003562](https://doi.org/10.1029/2009je003562).
- Tolosana-Delgado, R., von Eynatten, H., 2009. Grain-Size control on petrographic composition of Sediments: compositional regression and rounded zeros. *Math. Geosci.* 41, 869–886. doi:[10.1007/s11004-009-9216-6](https://doi.org/10.1007/s11004-009-9216-6).
- Viviano-Beck, C.E., et al., 2014. Revised CRISM spectral parameters and summary products based on the currently detected mineral diversity on mars. *J. Geophys. Res.-Planets* 119, 1403–1431. doi:[10.1002/2014je004627](https://doi.org/10.1002/2014je004627).
- Weltje, G.J., von Eynatten, H., 2004. Quantitative provenance analysis of sediments: review and outlook. *Sediment. Geol.* 171, 1–11. doi:[10.1016/j.sedgeo.2004.05.007](https://doi.org/10.1016/j.sedgeo.2004.05.007).
- Yen, A.S., et al., 2005. An integrated view of the chemistry and mineralogy of martian soils. *Nature* 436, 49–54. doi:[10.1038/nature03637](https://doi.org/10.1038/nature03637).